# CHARACTERISTICS OF THUNDERSTORMS THAT PRODUCE TERRESTRIAL GAMMA RAY FLASHES

BY THEMISTOKLIS CHRONIS, MICHAEL S. BRIGGS, GEORGE PRIFTIS, VALERIE CONNAUGHTON, JAMES BRUNDELL, ROBERT HOLZWORTH, STAN HECKMAN, SHELIA MCBREEN, GERARD FITZPATRICK, AND MATTHEW STANBRO

NEXRAD-enhanced echo-top data show that 24 terrestrial gamma ray flashes (TGF) detected with the Fermi Gamma Ray Burst Monitor (GBM) are consistently adjacent to high-altitude regions of storms.

Terrestrial gamma ray flashes (TGFs) are submillisecond-duration intense bursts of gamma rays readily detectable from low-Earth orbit (Fishman et al. 1994; Smith et al. 2005; Grefenstette et al. 2009; Marisaldi et al. 2014; Briggs et al. 2010, 2013). This emphasizes the extreme nature of the phenomenon: even when observed from hundreds of kilometers above the sources, the gamma ray fluxes are still strong enough to saturate some gamma ray instruments (Grefenstette et al. 2008). TGFs and the emerging field of high-energy atmospheric physics are reviewed by Dwyer et al. (2012) and Dwyer and Uman (2014). The terrestrial origin was established by correlation with thunderstorms (Fishman et al. 1994); more recently observations associated TGFs with positive intracloud (+IC) lightning during upward leader propagation (Stanley et al. 2006; Williams et al. 2006; Lu et al. 2010; Shao et al. 2010).

Despite the recognition from their discovery that TGFs originate from thunderstorms (Fishman et al. 1994), relatively little is known about the storms that produce TGFs. Most research has focused on gamma ray and radio observations and theoretical investigations (>200 papers), with comparatively few papers on meteorological observations (Smith et al. 2010; Splitt et al. 2010; Lu et al. 2010; Barnes et al. 2015). Herein, we use 24 accurately geolocated TGFs that are within range of Next Generation Weather Radars (NEXRADs) to identify and study TGF-producing storms. We ask, "Do these 24 TGF-producing storms exhibit any distinct convective characteristics?"

TGFs start with the acceleration of electrons to relativistic energies by electric fields in thunderstorms, either in large-scale high-field regions of thunderstorms (Dwyer 2008) or in the smaller high-field regions of lightning leaders (Carlson et al. 2010; Celestin and Pasko 2011). The TGF gamma rays are produced by bremsstrahlung from these energetic electrons when they are deflected by passing near atomic nuclei (Dwyer et al. 2012). Electrons are said to "run away" when the rate of energy gain from the electric field exceeds their energy losses from interactions with the ambient air (Dwyer et al. 2012). Electron–electron scattering can increase the number of runaway

electrons, leading to avalanches of electrons (Gurevich et al. 1992). Backscattered gamma rays and positrons produced by pair production from gamma rays can produce additional seed electrons at the start of the acceleration region, causing positive feedback and multiplication of avalanches (Dwyer 2003, 2007).

TGFs are detected at offsets from the spacecraft nadirs of up to ~800 km (Lay 2008; Cohen et al. 2010; Collier et al. 2011; Connaughton et al. 2013; Briggs et al. 2013). This has hindered studies of the meteorology of TGF storms since there are likely to be multiple storms within each TGF detection region, precluding the identification of the TGF-producing storm. Two studies used lightning detections by the World Wide Lightning Location Network (WWLLN) to find cases in which there were likely only single storms within the detection region of the Reuven Ramaty High Energy Solar Spectroscopic Imager (RHESSI) gamma ray instrument, so that those storms could be definitely associated with TGFs (Smith et al. 2010; Splitt et al. 2010). Smith et al. (2010) identified 51 single storms from a sample of 619 TGFs. They summed the WWLLN flash rate histories, aligned at the TGF occurrence times, and found a decreasing flash rate, suggesting that TGFs occur during the decline of flash production.

Splitt et al. (2010) estimated cloud-top heights for 29 single-storm cases from geostationary satellite brightness temperatures, finding values ranging from 13.6 to 17.3 km, with an average of 15.3 km. These values are typical for tropical deep convective systems (Liu et al. 2008). A relative deficiency of TGFs from midlatitudes, where cloud-top heights are typically lower, suggests that the gamma rays from TGFs from lower clouds are sufficiently attenuated by the denser atmosphere that these TGFs are less likely to be detected from space (Williams et al. 2006; Smith et al. 2010; Splitt et al. 2010). Similarly cloud-top temperatures were used to estimate cloud-top area. The 29 single-storm cases had a very wide range of areas, with a possible preference for larger areas (Splitt et al. 2010). Expanding the sample beyond single-storm cases, surface convective available potential energy (CAPE) was evaluated for the regions underneath RHESSI at the times of 805 TGFs. While the TGF regions sampled a wide range of CAPE values, there was a clear preference for larger values compared to the CAPE values for random tropical regions selected independently of whether the regions contained storms (Splitt et al. 2010).

Barnes et al. (2015) used data from two instruments on the Tropical Rainfall Measuring Mission (TRMM) to study the storms related to RHESSI TGFs. Regions with storms were identified with lightning detections from the Lightning Imaging Sensor (LIS) on board TRMM. Regions were included in the samples if the spacecraft nadirs were within 500 km and the observations were within 1 h. Two samples were created, TGF and non-TGF control, based on whether RHESSI detected a TGF. The TRMM Microwave Imager (TMI) was used to compare the hydrometeor content of the storms within the two samples. Despite the limitations that the TGF location might not be within the field of view of the TMI, that the field of view might contain multiple storms, and that the storm may have evolved between the time of the TGF and the observation with the TMI, clear differences in the hydrometeor content of the two samples were found. The TGF regions contained higher concentrations of cloud water and ice and precipitation water and ice.

The most detailed meteorological observations of a TGF are those of the TGF detected by RHESSI over Tennessee on 26 July 2008. The storm and lightning were observed with the North Alabama Lightning Mapping Array (Goodman et al. 2005), ground-based weather radar, and other sensors. The cloud had a strong updraft, with the cloud top between 13 and 16 km. The TGF was related to an IC flash that occurred between a negative charge layer at 8.5 km and a positive charge layer at 13 km (Lu et al. 2010).

Numerous radio observations have been made of TGF-producing storms, with the radio signals

**AFFILIATIONS:** Chronis—Earth System Science Center, University of Alabama in Huntsville, Huntsville, Alabama; Briggs, Connaughton, and Stanbro—Center for Space Plasma and Aeronomic Research, University of Alabama in Huntsville, Huntsville, Alabama; Priftis—Department of Atmospheric Science, University of Alabama in Huntsville, Huntsville, Alabama; Brundell—Department of Physics, University of Otago, Dunedin, New Zealand; Holzworth—Department of Earth and Space Sciences, University of Washington, Seattle, Washington; Heckman—Earth Networks, Germantown, Maryland; McBreen and Fitzpatrick—School of Physics, University College Dublin, Belfield, Dublin, Ireland
**CORRESPONDING AUTHOR:** Themistoklis Chronis, ESSC, University of Alabama in Huntsville, 301 Sparkman Dr. NW, Huntsville, AL 35899
E-mail: themis.chronis@nsstc.uah.edu

*The abstract for this article can be found in this issue, following the table of contents.*
DOI:10.1175/BAMS-D-14-00239.1

A supplement to this article is available online (10.1175/BAMS-D-14-00239.2)

In final form 11 June 2015

originally interpreted as TGF-associated lightning processes (Inan et al. 1996; Cummer et al. 2005; Stanley et al. 2006; Cohen et al. 2006; Inan et al. 2006; Lay 2008; Cohen et al. 2010; Shao et al. 2010). Cummer et al. (2011) noted that the source current waveform of the radio signal had a similar temporal profile to the gamma ray light curve and suggested that the radio emission might originate from the gamma ray production. Many of the radio observations have been made in the very low-frequency (VLF) range because these signals undergo little attenuation, propagating in the Earth–ionosphere waveguide, and can be detected thousands of kilometers from the source (Price 2008). These observations are particularly useful for wide geographic coverage TGF samples. The first studies were unable to determine the temporal order of the gamma ray and radio signals, limited by the timing accuracy of RHESSI (Grefenstette et al. 2009). Using the several-microsecond absolute timing accuracy of the Fermi Gamma Ray Burst Monitor (GBM), Connaughton et al. (2010) found that most GBM TGF/WWLLN associations were simultaneous within ±40 $\mu$s (after correcting for light travel time between the two observations), but there are also statistically significant associations with millisecond separations. For the simultaneous associations, Connaughton et al. (2013) found an extremely strong anticorrelation between the TGF duration and the probability of a GBM/WWLLN association, but no such correlation was found for the millisecond-scale associations. The explanation is that the millisecond-scale separations are due to associated IC processes, while the simultaneous associations are actually radio emission from the TGF itself. The frequency of the radio emission is a strong function of the TGF rise time, controlling whether (short TGFs) or not (long TGFs) the radio emission is within the passband of WWLLN (Dwyer and Cummer 2013). These TGF-produced radio signals are some of the strongest signals detected with WWLLN (Connaughton et al. 2013).

For the first decade after their discovery, TGFs were generally thought to originate in the upper atmosphere, motivated by perceived connections to transient luminous events such as sprites and because a high altitude reduces the attenuation of the gamma rays (Dwyer et al. 2012). The observation from ground of a short gamma ray burst from a thunderstorm suggested that a similar event could be observable from space (Dwyer et al. 2004). An analysis of the summed spectra of 289 TGFs observed with RHESSI for the amount of atmosphere traversed by the gamma rays indicated a source altitude of 15–21 km (Dwyer and Smith 2005). Other works comparing TGF spectra to beaming models tended to favor altitudes of ~15 km (Dwyer et al. 2012). Radio observations of lightning associated with RHESSI TGFs showed the lightning charge moment changes to be too small to create the high-altitude electric fields required for models of high-altitude TGFs (Dwyer et al. 2012). The interpretation of the latitude distribution of TGFs (i.e., deficiency at midlatitudes attributed to lower cloud tops; see above) is based on the TGF sources being in or very close to thunderclouds. These results and observations closely associating TGFs with +IC lightning (see above) changed the general view toward TGF sources being located in or very close to thunderclouds (Dwyer et al. 2012). Recent observations of radio signals simultaneous with two GBM TGFs, with the radio signals therefore originating from the TGF process rather than from lightning, determined source altitudes of 11.8 ± 0.4 km and 11.9 ± 0.9 km (Cummer et al. 2014). These analyses of TGF source altitudes are based on TGFs detected by spaced-based instruments such as RHESSI or GBM; those instruments may be detecting only the highest and thus least attenuated sources, which is suggested by the latitude distribution.

Analysis of TGF-producing storms has been limited both by the difficulty in identifying these storms and by the paucity of ground-based meteorological observations, especially in the tropics, where TGFs are most frequent. This study takes advantage of improved TGF detection efficiencies, by both Fermi GBM and ground-based lightning detection systems, and results in a unique sample of 24 well-geolocated TGFs over the Gulf of Mexico, the Caribbean, and the west Pacific that are within the operational range of the NEXRAD ground-based network. Our goal is to explore detailed meteorological observations of the storms that produced these TGFs.

**DATA.** *Fermi GBM.* The GBM on the Fermi Gamma Ray Space Telescope was designed for astrophysics, primarily to observe cosmic gamma ray bursts. GBM detects gamma rays with 14 scintillation detectors of two types to cover the energy range from 8 keV to 40 MeV. The detectors detect gamma rays from all directions not blocked by the spacecraft, with even some sensitivity through the spacecraft, and do not measure the directions of individual photons. Gamma ray bursts can be localized to several degrees of accuracy by comparing the detector rates, but this technique does not work well for TGFs (Meegan et al. 2009; Briggs et al. 2010). From launch in 2008 GBM was detecting one TGF per month. Because of a series of data and analysis improvements (Briggs et al. 2013),

since November 2012 the rate is improved to ~800 $yr^{-1}$, resulting in a sample through 2013 of 2,279 TGFs.

*VLF radio geolocations and the storm sample.* Correlating this TGF sample with radio detections of WWLLN and the Earth Networks Total Lighting Network (ENTLN) (Liu and Heckman 2010), 877 TGF/radio associations are obtained (38% association rate). The high association rate is the result of improvements to these networks over the past few years (Rodger et al. 2009; Hutchins et al. 2012). Typical uncertainty radii range between 5 and 10 km (Liu and Heckman 2010; Hutchins et al. 2012). Specific elliptical uncertainty regions for each TGF detected with WWLLN are calculated by Monte Carlo simulations of the uncertainties of the time of group arrival measurements at the participating stations. For ENTLN, we conservatively use 10-km radii.

We choose to use VLF geolocations because of their high accuracy and the large fraction of the TGF sample for which they are available. In contrast, so far there is no GBM–LIS association [there are only two RHESSI–LIS (Østgaard et al. 2013; Gjesteland et al. 2015)], nor are there any GBM–Lightning Mapping Array (LMA) detections [there is only one RHESSI–LMA (Lu et al. 2010)]. We find it rare to identify useable single storms from sferic (lightning radio signal) maps, with WWLLN or ENTLN sferic maps of regions in which the TGFs could have originated (i.e., within 800 km of the nadir of Fermi) for ±10 min about the TGF times typically showing many clusters or clusters with large extents (see Figs. ES1–ES4 for four examples; more information can be found online at http://dx.doi.org/10.1175/BAMS-D-14-00239.2). Examining 834 WWLLN sferic maps for TGFs with GBM/WWLLN associations, for only ~1% of the maps could a geolocation be determined based on the sferics being within a ~100-km radius circle. Earlier investigations found a higher "single storm" rate (Smith et al. 2010; Splitt et al. 2010), perhaps because at that time WWLLN had a lower detection efficiency (Rodger et al. 2009) or because a 600-km radius search region was used instead of 800 km.

The intersection of the sample of 877 well-geolocated TGFs with the coverage of the NEXRAD network results in a sample of 24 TGF-producing storms observed from nine NEXRAD stations in Florida, Louisiana, Texas, Puerto Rico, and Guam (Fig. 1; Tables ES1–ES2). In some respects this sample is similar to the known TGF population, which is "frequent near coastlines, large islands, peninsulas, and isthmuses" (Splitt et al. 2010); these 24 TGFs are near such features, with the median distance from coastline being 28 km. On a larger scale, the requirement for a Fermi GBM detection places most of the 2,279 TGFs under the orbit of Fermi (25.6° inclination), with a few detected at higher latitudes due to the ~800-km detection radius. Adding the requirement of being within range of a NEXRAD station limits the final sample to one near Guam (+14.7° latitude) and 23 in and near the Gulf of Mexico and the Caribbean (latitudes +16.9° to +29.3°, mean +24.2°) (Table ES1). This contrasts with the TGF latitude distribution found with RHESSI (38° inclination orbit), which shows that most TGFs are within ±20° latitude (Smith et al. 2010). Figure 1 can also be compared to "global" TGF maps (e.g., Grefenstette et al. 2009; Splitt et al. 2010; Gjesteland et al. 2012; Briggs et al. 2013). While the sample is similar, compared to the overall TGF population, in its proximity to geographic features, its limited geographic range might cause a bias in the types and characteristics of the storms. Because of the requirement for a VLF geolocation, the sample is strongly biased toward shorter TGFs (Connaughton et al. 2013); while we know of no reason that the properties of the TGF-producing storm should correlate with TGF duration, there is no evidence on that topic.

Of the 24 TGFs, 21 have GBM/VLF associations that are within ±200 $\mu$s and are thus considered simultaneous, so that the radio signal is very likely from the TGF itself rather than from associated lighting processes (Table ES1). [The match between radio and gamma ray signals is made after correcting for the light travel time differences from the source. A ±200-$\mu$s window is used to test for simultaneity rather than the ±40-$\mu$s window of Connaughton et al. (2010) because the TGF peak times are determined less accurately for this large sample.] The search for associations was conducted with an 800-km radius and ±3.5-ms window. The probability of a chance association with background sferics is found by applying the procedure at control times offset from the TGF time. Associations are accepted if the chance probability is less than 1% for WWLLN and 10% for ENTLN. A higher screening probability is necessary for ENTLN stroke data because of the high ambient rate of ENTLN strokes due to the sensitivity of ENTLN to IC lightning and the ability of ENTLN to detect multiple strokes per flash. When an association is found within ±200 $\mu$s of the TGF, the chance association probability becomes ×3.5/0.2 smaller, that is, less than 0.6% for ENTLN; this applies for 15 of the 17 ENTLN associations. The only TGF that has only an ENTLN association, which is nonsimultaneous, is TGF111101122, which has a chance association probability based on the ambient ENTLN stroke rate of 2.9%. All other associations

have chance probabilities of less than 1%, typically much less because they are within the smaller ±200-$\mu$s window.

Since in most cases the radio signal is from the TGF itself, the differing efficiencies of WWLLN and ENTLN for detecting IC lighting are not pertinent. For the 21 TGFs that have simultaneous VLF associations, the signal is very likely from the TGF itself and thus the radio geolocation is directly a TGF geolocation. There are fewer common millisecond-scale associations that are attributed to associated IC lightning. Analysis of TGFs that have two or more associated ENTLN signals, with a simultaneous (i.e., TGF interpretation) signal and nonsimultaneous signal(s) (i.e., IC lightning interpretation), finds close separations between the several geolocations per TGF, consistent with the localization uncertainties (S. Xiong et al. 2015, unpublished manuscript). Thus, we may also use VLF geolocations from nonsimultaneous associations (or the occasional IC lightning signal within ±200 $\mu$s of the TGF) as geolocations of TGFs.

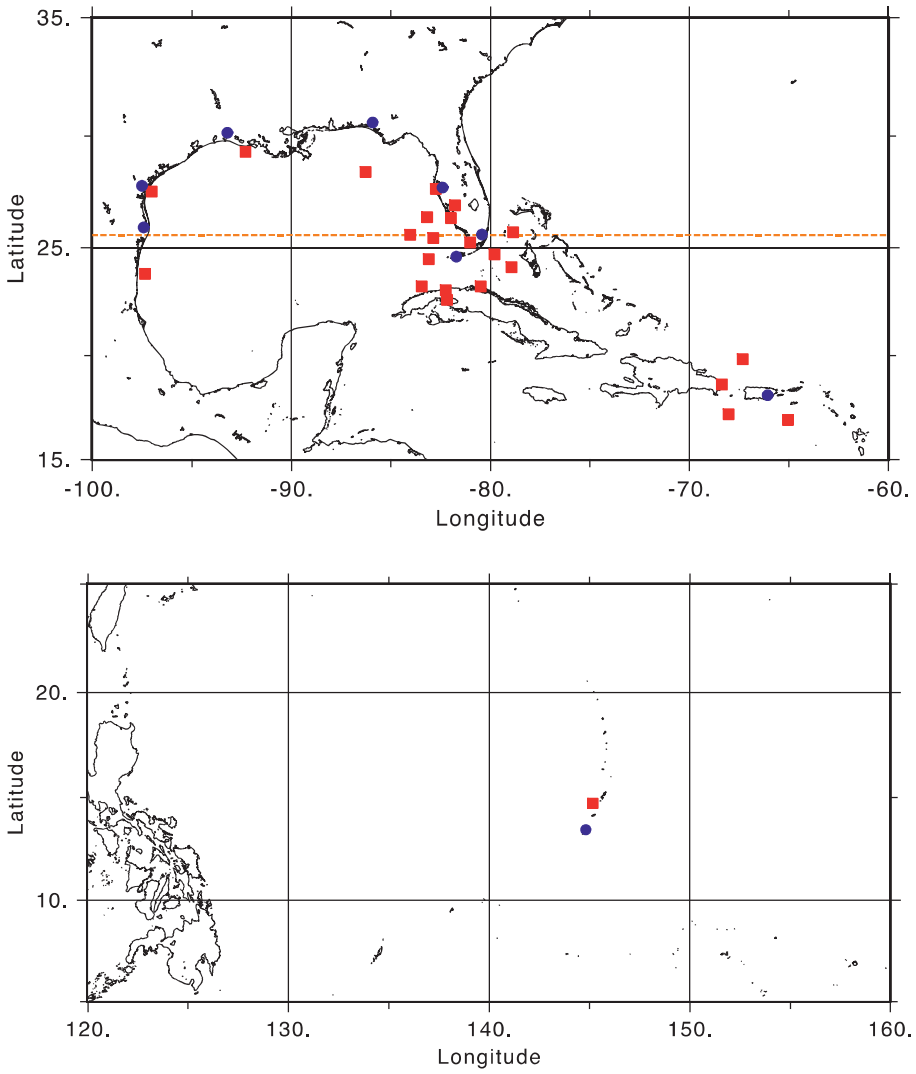


**Fig. 1. Maps of the 24 TGF locations (red squares; WWLLN or ENTLN) and the NEXRAD stations (blue circles) that observed the corresponding storms. The dashed orange line shows the northern limit of the orbit of Fermi; TGFs are detected past this limit, with decreasing probability with distance, due to the ≈800-km detection radius of GBM. Of the TGFs, 2 were over land, 17 were over ocean, and 5 were within 10 km of a coastline.**

*NEXRAD measurements.* The basic observation is the radar reflectivity $Z$ (in dB$Z$), from which several higher-level NEXRAD products are used as measures of the storm's convective characteristics. The $Z$ three-dimensional volume scan provides information on the storm's convective intensity. Typically, $Z$ values greater than ~20–30 dB$Z$ higher than ~6 km are a good indicator for the presence of mixed phase, cloud charge separation, and lightning production (Takahashi 1973; Saunders 1993; Zipser and Lutz 1994; Carey and Rutledge 2000). The constant-altitude plan position indicator (CAPPI) can be thought of as a horizontal "slice" of $Z$ along a constant altitude. We will report the altitude at which the maximum CAPPI is observed.

Two-dimensional radar proxies are more convenient in examining multiple storms. The enhanced echo tops (EET; in km) represent the maximum elevation at which the weakest $Z$ (~18 dB$Z$) is detected (Klazura and Imy 1993). Since a cloud's highest altitude is always higher than its ~18-dB$Z$ $Z$ level, EET is an underestimate of the "cloud top." Nevertheless, for the past few decades it has been considered to be an adequate proxy for identifying the overall storm's height distribution (Klazura and Imy 1993). Furthermore, the ratio between the EET and the vertically integrated liquid (VIL) results in the VIL density (VILD; in g m$^{-3}$), also a NEXRAD proxy that has been traditionally used as an indicator for updraft strength and hail production (Kitzmiller et al. 1995;

Amburn and Wolf 1997; Blaes et al. 1998). In general, storms with VILD values greater than ~2.5–3.0 g $m^{-3}$ have shown to sustain strong updrafts that produce hail larger than ~1 in. (see Lenning and Fuelberg 1998; Edwards and Thompson 1998; Cerniglia and Snyder 2002). Although there is no perfect metric for a storm's convective strength, VILD can distinguish relatively weaker (e.g., VILD = 0.5 g $m^{-3}$) from relatively stronger storms (e.g., VILD = 4.0 g $m^{-3}$). Because the TGF geolocation uncertainties, originating from the VLF network timing uncertainties, are larger than the spatial resolution of the NEXRAD data, we cannot simply select a single NEXRAD pixel per TGF. The analysis should take into account that the NEXRAD measurement (e.g., EET or VILD) corresponding to the TGF could be anywhere within the geolocation uncertainty region. We use two approaches: 1) accumulating EET and VILD values over the uncertainty regions of all of the TGFs (Figs. 2a–3a), and 2) considering EET and VILD values of each TGF, so that the "averaging" effect of 1 is reduced (Figs. 2b–3b; anonymous reviewers 2015, personal communication). Figures 2b–3b are also known as box-and-whisker plots and show the minimum, 25% quartile, median, 75% quartile, and maximum values of the variables (also see Table 1). For the EET and VILD analyses, we do not include pixels that are lower than 6.5 km; that is, we do not use pixels that do not include the mixed phase where the main charge separation occurs (e.g., Carey and Rutledge 2000).

All NEXRAD data are provided by the National Oceanic and Atmospheric Administration (NOAA) National Climatic Data Center (NCDC). The *Z* volume scans are provided as level-2 data and are displayed using the Gibson Ridge Level-2 Analyst Edition (GR2AE). GR2AE can only display data on a square grid and altitudes in kilofeet. The EET and VILD are provided as level-3 products at 1° × 1-km polar grid resolution. Both variables are mapped using the NOAA Weather and Climate Toolkit (Ansari et al. 2009). All NEXRAD products were obtained at the radar sampling (available at ~5-min intervals) closest to the TGF time and are in precipitation mode (14 elevation scanning angles).

*CAPE.* We obtain the surface CAPE values from the NCEP North American Regional Reanalysis (NARR). NARR offers the opportunity for spatial (≈32 km) and temporal (8 times daily) high-resolution reanalysis datasets (Mesinger et al. 2006) and has served as the main data source for severe weather climatology studies over the United States (see Gensini and Ashley 2011). CAPE (J $kg^{-1}$) is a thermodynamic variable indicative of the maximum potential vertical speed (i.e.,

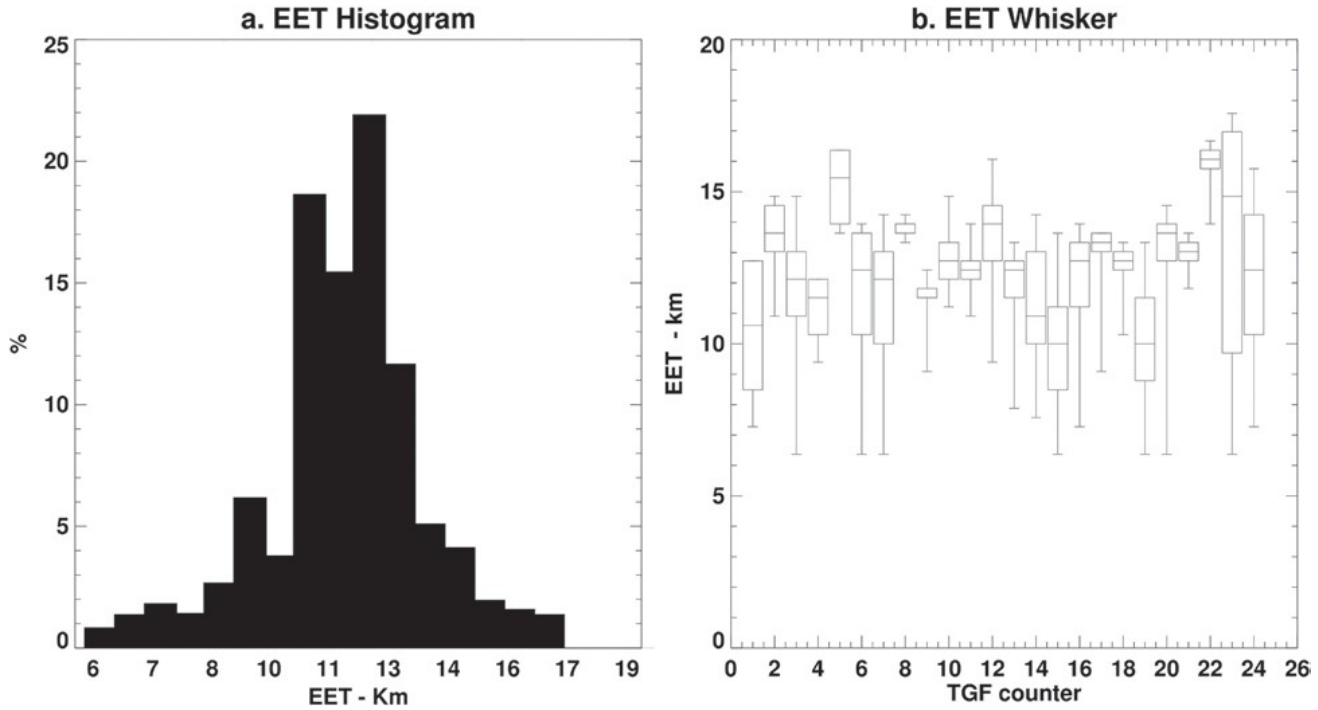


**Fig. 2. (a) EET (km) histogram around all 24 TGFs. The values are accumulated over the geolocation uncertainty regions, for pixels ≥ 6.5 km. (b) Box-and-whisker plot for EET (km) for each of the TGFs. The vertical lines extend to the minimum and maximum EET values. Values below 6 km are excluded. The boxes extend from the 25% to the 75% quartiles, with a horizontal line at the median values.**

updraft) of a rising air parcel. Although substantial discrepancies between CAPE values and measured updraft speeds are observed (i.e., parcel theory), high CAPE is synonymous with the potential for severe storm development (Williams et al. 2005). In this paper, EET, VILD, *Z* volume scans, CAPPI, and CAPE will be synergistically employed to address the following question: "What are the convective characteristics of TGF-producing storms?"

**RESULTS.** The EET values accumulated over the TGF uncertainty regions exhibit a unimodal distribution with median value ~11–13 km (Fig. 2a). About 75%–80% of these EET values are higher than ~10 km. Individual EET values around each TGF (Fig. 2b) are also consistent with this picture. For instance, the 25% percentiles for 20 out of 24 TGFs are higher than 10 km (Fig. 2b; i.e., 75% of the EET NEXRAD pixels within the TGF uncertainty region are higher than 10 km). In addition, all 24 TGFs exhibit median values above ~10 km. The maximum EET values for every TGF in the sample are above ~12 km, whereas the minimum EET values can range from ~6 to 14 km (the minimum of 6.5 km is imposed by the pixel criteria).

The range of EET values within a TGF uncertainty region may indicate different storm features. For example, TGF110801123 (see Table 1; Figs. 2b and ES6) has a small range of EET values (~1 km between minimum and maximum), indicating that the TGF region encompasses an area within the storm of uniform cloud top. Cases such as TGF130713734, TGF120421334, TGF130701021, and TGF131030234 that exhibit large (~2 km) differences between the 75% quartile and maximum EET values within the TGF geolocation uncertainty region (e.g., see Table 1; Figs. 2b and ES5–ES10) could suggest the presence of overshooting parts in the storm (anonymous reviewer 2015, personal communication).

Although the TGF uncertainty region includes parts of the storm that are strictly unrelated to the TGF production, the respective distribution shown in Fig. 2 suggests that the TGF-associated EETs are above ~12 km. In line with the aforementioned, the EET 2D maps (Figs. ES5–ES10) reveal that the TGF uncertainty regions include some of the highest parts of the encompassing storms but not necessarily the single highest part of each respective storm. As in Fig. 2, Table 1 summarizes the EET distribution values for all 24 TGFs.

The modal VILD value from all 24 TGFs (Fig. 3a) is ~1.0 g m$^{-3}$. Interestingly, the VILD values within the uncertainty region around each TGF (Fig. 3b) indicate storms with a variety of convective strengths, with

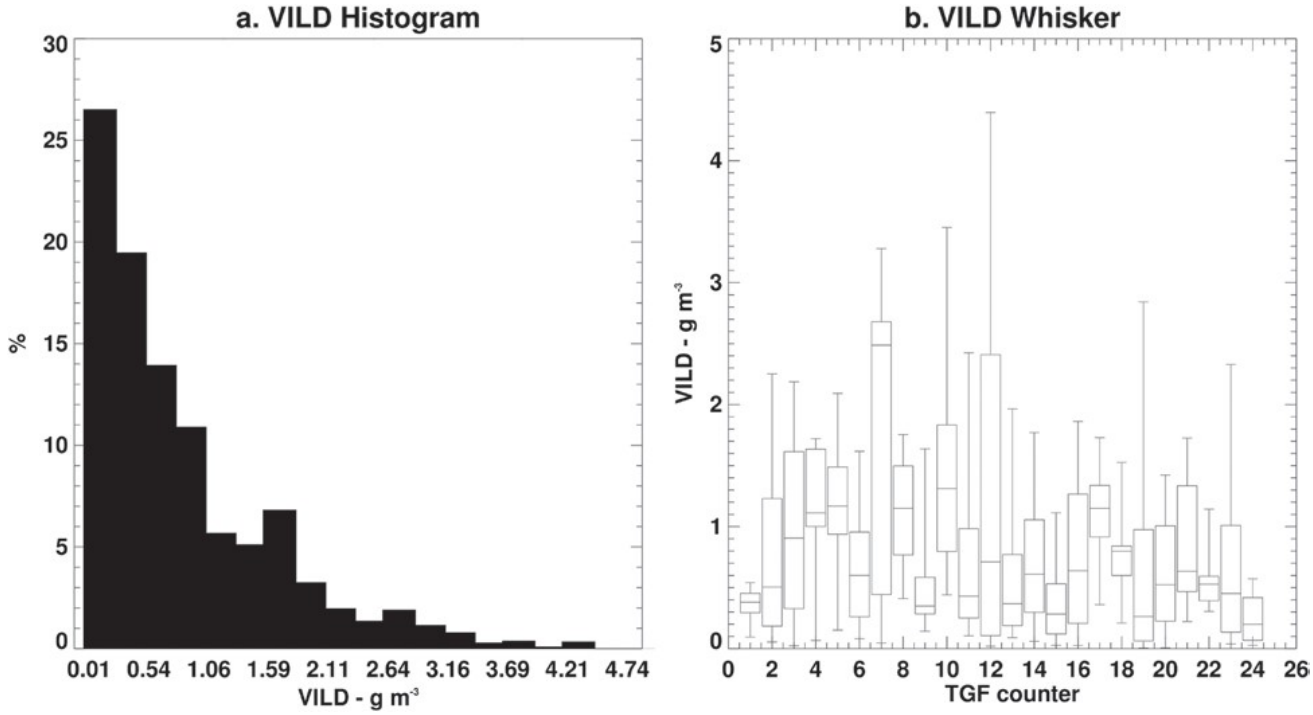


**Fig. 3. (a) VILD (g m$^{-3}$) histogram around all 24 TGFs. The values are accumulated over the geolocation uncertainty regions, for pixels with EET values ≥ 6.5 km. (b) Box-and-whisker plot for VILD (g m$^{-3}$) for each of the TGFs. The vertical lines extend to the minimum and maximum EET values. The boxes extend from the 25% to the 75% quartiles, with a horizontal line at the median values.**

median values ranging from 0.20 to 2.49 g $m^{-3}$ (see Fig. 3b and Table 1). As with EET, there are substantial differences between minimum and maximum VILD values within the TGF uncertainty regions. Larger differences likely pertain to the TGF geolocation uncertainty region encompassing the main convective core and some of the stratiform parts of the storm. Although one could argue that all 24 TGFs originate from the maximum VILD values (see Table 1), the claim of storm "variety" can still be made given the range of maximum VILD values (e.g., relatively weaker convection with VILD = 0.54 g $m^{-3}$) or relatively stronger convection with VILD = 4.40 g $m^{-3}$; see Fig. 3b and Table 1).

In agreement with the findings in Figs. 3a and 3b, the VILD maps for the individual TGFs (Figs. ES11–ES16) suggest that the TGF-producing storms can range from scattered weak convection (e.g., TGF100803822 and TGF130809149; Fig. ES11) to more organized (e.g., multicell) and relatively deeper convection (e.g., TGF120421334 or TGF130607515; see Fig. ES13). As in Fig. 3, Table 1 summarizes the VILD distribution values for all 24 TGFs.

Here, we examine the *Z* volume scans for four TGFs in detail; the *Z* volume scan plots for all 24 TGFs can be found in the supplemental information in Figs. ES17–ES22. TGF130607515 (Fig. 4a) represents a case of relatively deeper convection (i.e., at least with respect to the rest of our sample), with the 50–60 dB*Z* extending up to ~6 km and the weakest detected *Z* (~10–20 dB*Z*) observed above ~13 km. The maximum CAPPI *Z* is computed as 62.5 dB*Z* at ~6-km altitude. This storm

**Table 1. EET, VILD, CAPPI, and CAPE statistics in the uncertainty regions of the 24 TGFs. EET and VILD are analyzed for pixels with EET ≥ 6 km. The sequential number (1–24) is used in Figs. 2b and 3b instead of the TGF name for clarity. The last three columns provide comparison CAPE values (minimum, mean, and median) obtained for the location and time of day of the TGF, averaged over the month in which the TGF occurred.**

| | TGF ID | NEXRAD | EET median (km) | EET min/max (km) | VILD median (g $m^{-3}$) | VILD min/max (g $m^{-3}$) |
|---|---|---|---|---|---|---|
| 1 | TGF100803822 | KAMX | 10.61 | 7.27/12.73 | 0.38 | 0.09/0.54 |
| 2 | TGF130520833 | KAMX | 13.64 | 10.92/14.85 | 0.50 | 0.05/2.25 |
| 3 | TGF130713734 | KAMX | 12.12 | 6.5/14.85 | 0.91 | 0.02/2.19 |
| 4 | TGF130809149 | KAMX | 11.52 | 9.39/12.12 | 1.11 | 0.07/1.72 |
| 5 | TGF130611560 | KBRO | 15.45 | 13.64/16.36 | 1.17 | 0.15/2.09 |
| 6 | TGF100916059 | KBYX | 12.42 | 6.5/13.94 | 0.60 | 0.08/1.62 |
| 7 | TGF110626928 | KBYX | 12.12 | 6.5/14.24 | 2.49 | 0.05/3.28 |
| 8 | TGF110801123 | KBYX | 13.94 | 13.33/14.24 | 1.15 | 0.41/1.75 |
| 9 | TGF111101122 | KBYX | 11.52 | 9.09/12.42 | 0.35 | 0.14/1.64 |
| 10 | TGF120421334 | KBYX | 12.73 | 11.21/14.85 | 1.31 | 0.44/3.45 |
| 11 | TGF130606592 | KBYX | 12.42 | 10.91/13.94 | 0.42 | 0.10/2.42 |
| 12 | TGF130607515 | KBYX | 13.94 | 9.39/16.06 | 0.71 | 0.02/4.40 |
| 13 | TGF110929773 | KCRP | 12.42 | 7.88/13.33 | 0.37 | 0.09/1.96 |
| 14 | TGF130925226 | KEVX | 10.91 | 7.58/14.24 | 0.61 | 0.06/1.77 |
| 15 | TGF120713614 | KLCH | 10.00 | 6.5/13.64 | 0.28 | 0.03/1.11 |
| 16 | TGF100807804 | KTBW | 12.73 | 7.27/13.94 | 0.64 | 0.03/1.86 |
| 17 | TGF110830487 | KTBW | 13.33 | 9.09/13.64 | 1.15 | 0.36/1.73 |
| 18 | TGF130630951 | KTBW | 12.73 | 10.30/13.33 | 0.80 | 0.21/1.53 |
| 19 | TGF130701021 | KTBW | 10.00 | 6.5/13.33 | 0.26 | 0.01/2.84 |
| 20 | TGF130905817 | PGUA | 13.64 | 6.5/14.54 | 0.52 | 0.01/1.42 |
| 21 | TGF110816556 | TJUA | 13.03 | 11.82/13.64 | 0.63 | 0.22/1.73 |
| 22 | TGF120731311 | TJUA | 16.06 | 13.94/16.67 | 0.53 | 0.31/1.14 |
| 23 | TGF130930128 | TJUA | 14.85 | 6.5/17.58 | 0.45 | 0.04/2.33 |
| 24 | TGF131030234 | TJUA | 12.42 | 7.26/15.76 | 0.20 | 0.03/0.57 |

exhibits EET and VILD values ranging from 9.39 to 16.06 km and 0.02 to 4.4 g $m^{-3}$, respectively (median values are 13.94 km and 0.71 g $m^{-3}$, respectively; see Table 1). The associated CAPE value is 2,630 J $kg^{-1}$. To provide a comparison to this CAPE value, we also compute the minimum, mean, and maximum CAPE values for all days of the month at the same location and time of day. For June 2013 at 1200 UTC (see Table 1) the minimum, mean, and maximum CAPE values are 700, 2,640, and 4,650 J $kg^{-1}$, respectively. Hence, a CAPE value of 2,630 J $kg^{-1}$ could be characterized as a storm with an "average" monthly CAPE.

TGF130630951 (Fig. 4b) illustrates an example of a relatively shallower convection (i.e., compared to the previous example), with the 30–40-dB*Z* level reaching ~6 km, delineating the updraft of the southern storm cell. The maximum CAPPI *Z* is found ~48.5 dB*Z* at ~3-km altitude. The minimum detectable *Z* (~10–20 dB*Z*) is also well above 10 km, in line with the EET values that range from ~10.3 to 13.3 km with a median around 12.7 km. The respective maximum VILD values are computed as 1.53 g $m^{-3}$, with a median of 0.8 g $m^{-3}$ (see Table 1). The associated CAPE value is 1,400 J $kg^{-1}$. The respective monthly minimum, mean, and maximum CAPE values for June 2013 at 0000 UTC (see Table 1) are 590, 2,489 and 3,900 J $kg^{-1}$.

TGF111101122 (Fig. 4c) is the only winter storm in our sample, with the 30–40 and 20–30 dB*Z* stratified between ~6 and 7 km and 9 and 11 km, respectively (Fig. 4c). The maximum CAPPI *Z* is ~47.5 dB*Z* at ~4-km altitude. This storm exhibits EET and VILD values ranging

| | TGF ID | Altitude at $Z_{max}$ (m/dB*Z*) | CAPE (J $kg^{-1}$) | CAPE min (J $kg^{-1}$) | CAPE mean (J $kg^{-1}$) | CAPE max (J $kg^{-1}$) |
|---|---|---|---|---|---|---|
| 1 | TGF100803822 | 5,000/38 | 2,310 | 1,080 | 2,953 | 4,780 |
| 2 | TGF130520833 | 3,000/55 | 2,740 | 0 | 1,534 | 3,140 |
| 3 | TGF130713734 | 4,000/50 | 1,320 | 1,050 | 2,467 | 4,060 |
| 4 | TGF130809149 | 5,000/46 | 1,490 | 1,490 | 2,996 | 4,750 |
| 5 | TGF130611560 | 5,000/41.5 | 900 | 850 | 2,852 | 3,950 |
| 6 | TGF100916059 | 6,000/45 | 3,590 | 1,130 | 2,649 | 4,380 |
| 7 | TGF110626928 | 5,000/55.5 | 3,060 | 810 | 2,750 | 3,750 |
| 8 | TGF110801123 | 6,000/46 | 1,320 | 860 | 2,250 | 4,260 |
| 9 | TGF111101122 | 4,000/47.5 | 660 | 100 | 971 | 1,860 |
| 10 | TGF120421334 | 4,000/62 | 400 | 0 | 1,040 | 3,220 |
| 11 | TGF130606592 | 4,000/52.5 | 1,390 | 850 | 2,343 | 4,700 |
| 12 | TGF130607515 | 6,000/62.5 | 2,630 | 700 | 2,640 | 4,650 |
| 13 | TGF110929773 | 3,000/50 | 4,880 | 0 | 2,272 | 4,880 |
| 14 | TGF130925226 | 6,000/37.5 | 1,780 | 740 | 1,997 | 3,630 |
| 15 | TGF120713614 | 3,000/42 | 2,190 | 1,160 | 2,851 | 4,660 |
| 16 | TGF100807804 | 3,000/52.5 | 1,990 | 900 | 1,894 | 3,230 |
| 17 | TGF110830487 | 3,000/56 | 4,240 | 1,320 | 3,218 | 5,050 |
| 18 | TGF130630951 | 3,000/48.5 | 1,400 | 590 | 2,489 | 3,900 |
| 19 | TGF130701021 | 5,000/54 | 1,220 | 970 | 2,312 | 3,570 |
| 20 | TGF130905817 | — | — | — | — | — |
| 21 | TGF110816556 | 4,000/51 | 2,730 | 1,620 | 2,927 | 4,190 |
| 22 | TGF120731311 | 4,000/47 | 2,160 | 1,570 | 3,136 | 4,700 |
| 23 | TGF130930128 | 6,000/56 | 4,550 | 1,150 | 2,938 | 4,550 |
| 24 | TGF131030234 | 6,000/35 | 2,410 | 930 | 2,516 | 4,040 |

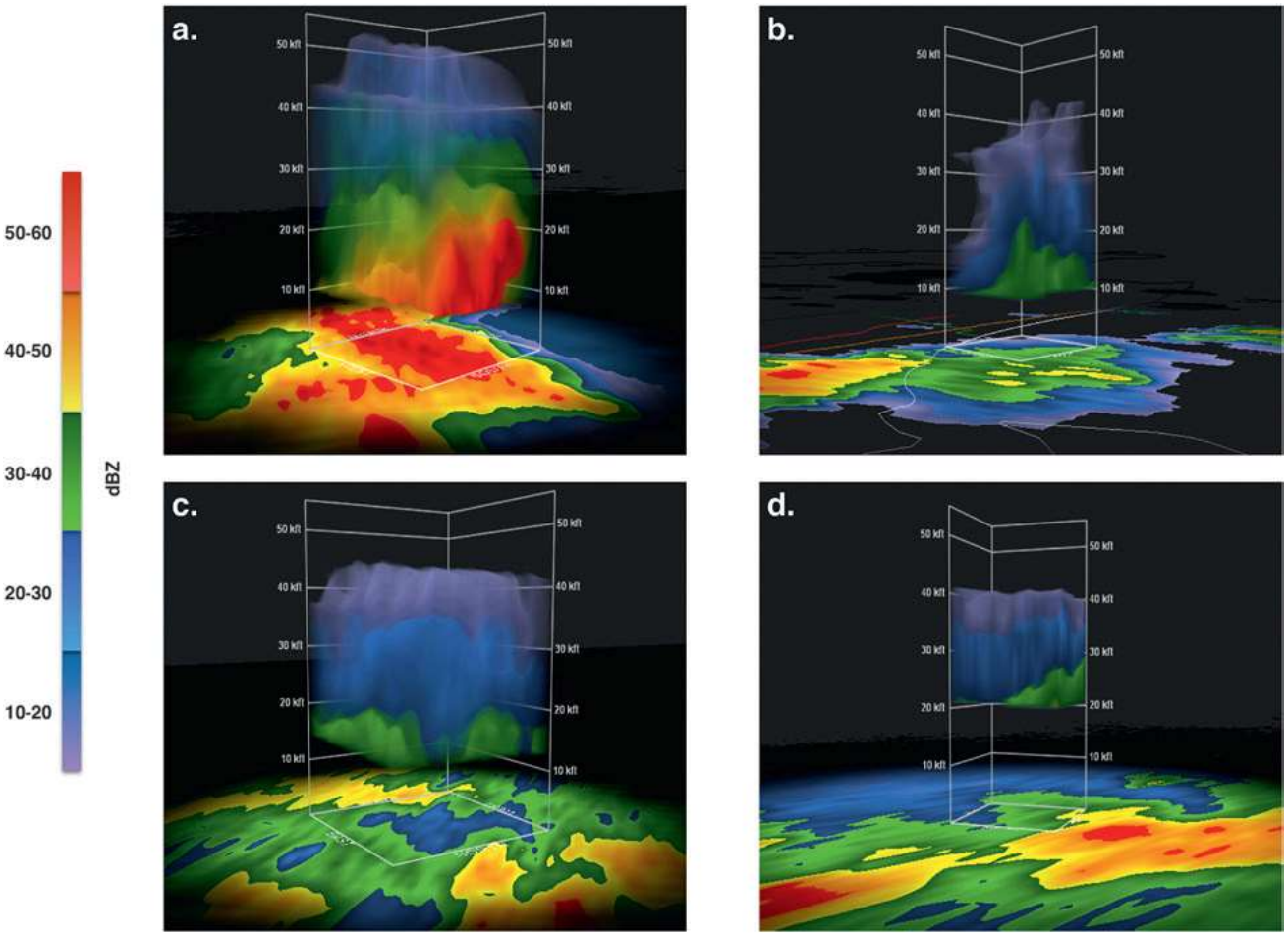


**Fig. 4. Three-dimensional reflectivity *Z* (dBZ) volume scans over a square grid of 10 by 10 km² that encompasses the locations of (a) TGF130607515, (b) TGF130630951, (c) TGF111101122, and (d) TGF130606592. Altitude is in kilofeet as output by GR2AE.**

from ~9.0 to 12.4 km and from 0.14 to 1.64 g m$^{-3}$, respectively (median values are 11.52 km and 0.35 g m$^{-3}$, respectively; see Table 1). The associated CAPE value is 660 J kg$^{-1}$. The respective monthly minimum, mean, and maximum CAPE values for November 2011 at 0300 UTC (see Table 1) are 100, 971, and 1,860 J kg$^{-1}$.

TGF130606592 (Fig. 4d) is associated with atmospheric instability from the presence of Tropical Cyclone Andrea in the Gulf of Mexico with the TGF located over the storm's rainband. It exhibits 30–40 dBZ, extending between ~6 and 7 km and the weakest (~10–20 dBZ) detectable *Z* at about 12 km. The maximum CAPPI *Z* is ~52.5 dBZ around 4 km. In line with the above, the EET values range from ~10.91 to 13.94 km with a median around 12.42 km (see Table 1). The respective maximum VILD values are computed as 2.42 g m$^{-3}$, with a median around 0.4 g m$^{-3}$. The associated CAPE value is 1,390 J kg$^{-1}$. The respective monthly minimum, mean, and maximum CAPE values for June 2013 at 1500 UTC (see Table 1) are 850, 2,343, and 4,700 J kg$^{-1}$.

Table 1 summarizes, among others, the CAPPI and CAPE and values for all 24 TGFs. No CAPE or *Z* data are available for TGF130905817 near Guam. CAPPI values throughout our sample are consistent with the observations pertaining to the VILD, in that TGF-producing storms span from relatively deeper to relatively shallower convection. Also, a wide range of CAPE values are observed, similar to Splitt et al. (2010); the values for the TGF storms are consistent with the values for other days of the months in which the TGFs occurred.

No NEXRAD product is bias free, and retrievals such as EET and VILD are dependent on parameters such as distance from the radar, storm propagating speed, and updraft structure (e.g., tilts) (DeLobbe and Holleman 2006; Howard et al. 1997; Setvák et al. 2010). For instance, because of the short distance of TGF130701021 from the KTBW NEXRAD (33 km; Table ES2), the EET/VILD retrievals may be underestimated, especially above ~11-km altitude due to the "cone of silence" effect (because of the ~19° tilt

NEXRAD angle) (anonymous reviewer 2015, personal communication). In addition, given the EET underestimation of the actual cloud-top heights, the inferred cloud-top heights in Fig. 2 should be shifted toward higher values that will consequently agree better with the observations in Splitt et al. (2010). Despite the caveats in interpreting the NEXRAD products, the consistency of the results herein supports the interpretation that a relatively higher EET value around the TGF location is a common characteristic, while conversely there is no standard convective strength. TGF130809149 (see Figs. ES5 and ES11), as well as many other TGFs found throughout the supplemental information, exemplifies the last argument. TGF130809149 is approximately 119 km (Table ES2) from the NEXRAD KAMX (Miami, Florida), and its geolocation uncertainty region nicely encompasses the main convective core of a relatively weak storm cell (Fig. ES11; VILD median = 1.1 g $m^{-3}$; maximum CAPPI $Z$ = 46 dB$Z$ at 5 km; Table 1), which is part of the scattered convection over the Gulf of Mexico. The EET 2D map for this storm (Fig. ES5) highlights that the TGF geolocation uncertainty region nicely outlines the higher parts of this storm.

*Summary.* Because the geolocation uncertainties are larger than the spatial resolution of the next NEXRAD data, we cannot identify the specific NEXRAD pixel that corresponds to each TGF. Instead, we "propagate the errors" by considering all of the NEXRAD measurements within the corresponding geolocation uncertainty regions. While this may dilute the results (i.e., compared to using only the most probable geolocation), it also accounts for the localization uncertainties.

Overall, the EET distribution for the TGF geolocation uncertainty regions shows a clear propensity for values higher than ~12 km (Fig. 2a). These cloud-top characteristics are common and consistent with satellite observations over the Gulf of Mexico and the Caribbean (Kokhanovsky et al. 2011; King et al. 2013; Liu et al. 2008; Ushio et al. 2001), that is, the regions that include 23 out of 24 TGFs in our sample. There is no known physical mechanism that would enforce TGFs to occur only near the high portions of these storms; hence, we attribute this observation to a selection effect. In particular, lower-altitude TGFs likely exist, but their gamma rays will be attenuated by the increased pathlength through the denser atmosphere, rendering most TGFs below the detection threshold of current spaced-based gamma ray detectors. This is consistent with the interpretation that TGFs are preferentially detected where the tropopause is higher (Williams et al. 2006; Smith et al. 2010). These ideas are very similar but distinct. The tropopause–altitude hypothesis seeks to explain why observed TGFs are strongly weighted to tropical storms (latitude distribution); we are seeking to explain the locations of TGFs within storms.

Regardless of the chosen VILD statistic (e.g., maximum, median, or 25% percentile), the VILD values in TGF geolocation uncertainty regions demonstrate that storms that are defined as (relatively) shallow or deep convection can still produce a TGF (Fig. 3; Table 1). The VILD-related findings are further supported by the $Z$ volume scans, CAPPI, and CAPE estimates, which also depict a variety of storms producing TGFs..

**CONCLUSIONS.** This examination of the convective characteristics of 24 TGF-producing storms finds a variety of convective strengths, ranging from relatively weaker to deeper convection, with no distinguishing characteristics. Follow-on studies with larger samples are needed to determine the "weakest" storm that is able to produce a TGF. For instance, the fact that the range of the VILD maxima has a lower bound of VILD = 0.54 g $m^{-3}$ (Fig. 3; Table 1) warrants additional research since this value might be biased by the preference of current spaced-based TGF instruments for high-altitude TGFs. While we have found that a wide range of storms can produce TGFs, studies with larger samples (see below) will determine whether TGFs are more likely from storms of particular convective strengths or types and can also investigate whether TGFs preferentially occur during particular storm phases.

A common finding for all 24 TGFs is the preference for the higher parts of the storm, likely due to a selection effect. As a result, calculations of the worldwide TGF rate that rely on scaling of the TGFs detected from space are likely underestimates. For example, correcting the observations for the limited portion of Earth observed by the spacecraft, the number of TGFs above the detection threshold of GBM and under the orbit of Fermi (i.e., between latitudes ±25.6°) was estimated as $4 \times 10^5$ $yr^{-1}$ (Briggs et al. 2013). Similarly, the ratio between GBM TGFs and lightning flashes optically detected by LIS and the Optical Transient Detector (OTD) (Boccippio et al. 2002; Christian et al. 2003) was estimated as 1:2,600 (Briggs et al. 2013). Because of the unknown number of low-altitude attenuated TGFs undetected by GBM and other current space-based gamma ray instruments, current estimates of the annual TGF rate and TGF/lightning ratio are lower limits.

The joint Fermi GBM and WWLLN/ENTLN sample continues to grow. Currently we are working

toward acquiring and postprocessing radar data from other regions worldwide so that we can check for regional dependencies of storm properties. The observations of the upcoming Geosynchronous Lightning Mapper (GLM) (Goodman et al. 2013), correlated with gamma ray instruments, will provide additional accurate TGF locations, along with new measurements of TGF-associated lightning. A Lightning Imaging Sensor (LIS) (Blakeslee et al. 2014) and the Atmosphere–Space Interaction Monitor (ASIM) (Neubert 2009) for TGFs will fly on the International Space Station, making simultaneous observations. The optically geolocated TGF samples (e.g., GBM/GLM and ASIM/LIS) will have the advantage of being unbiased with respect to TGF duration, unlike the radio-geolocated samples. While it seems unlikely that TGF storm properties correlate with TGF duration, the forthcoming optical geolocations will test this idea. We expect that these new observations will enhance our understanding of the relations between TGFs, lightning, and thunderstorms.

**ACKNOWLEDGMENTS.** The Fermi GBM Collaboration acknowledges support for GBM development, operations, and data analysis from the National Aeronautics and Space Administration (NASA) in the United States and from the Bundesministerium für Wirtschaft und Technologie (BMWi)/Deutsches Zentrum für Luft und Raumfahrt (DLR) in Germany. This work was supported in part by the Fermi Guest Investigator Program, Grants NNX11AE69G and NNX13AO89G. The first author acknowledges the support given by Dr. Steve Goodman, senior (chief) scientist, GOES-R System Program as part of the GOES-R Proving Ground and Risk Reduction programs. We thank Melissa Gibby and William Cleveland (Jacobs Engineering Group) for their efforts in detecting the GBM TGFs and Chris Schultz for the help with the NEXRAD interpretation. The authors thank Earth Networks for use of the ENTLN data and the World Wide Lightning Location Network (http://wwlln.net), a collaboration among over 50 universities and institutions, for use of the WWLLN data. The authors thank three anonymous reviewers for their thorough comments, which helped us greatly improve the paper.

## REFERENCES

Amburn, S. A., and P. L. Wolf, 1997: VIL density as a hail indicator. *Wea. Forecasting*, **12**, 473–478, doi:10.1175/1520-0434(1997)012<0473:VDAAHI>2.0.CO;2.

Ansari, S., C. Hutchins, S. D. Greco, N. S. Stroumentova, and M. Phillips, 2009: The weather and climate toolkit. Preprints, *25th Int. Conf. on Interactive Information and Processing Systems for Meteorology, Oceanography, and Hydrology (IIPS)*, Phoenix, AZ, Amer. Meteor. Soc., 6A.4. [Available online at https://ams.confex.com/ams/89annual/techprogram/paper_146485.htm.]

Barnes, D. E., M. E. Splitt, J. R. Dwyer, S. Lazarus, D. M. Smith, and H. K. Rassoul, 2015: A study of thunderstorm microphysical properties and lightning flash counts associated with terrestrial gamma-ray flashes. *J. Geophys. Res. Atmos.*, **120**, 3453–3464, doi:10.1002/2014JD021495.

Blaes, J. L., C. S. Cerniglia Jr., and M. A. Caropolo, 1998: VIL density as an indicator of hail across eastern New York and western New England. NOAA/National Weather Service Forecast Office Eastern Region Tech. Attachment 98-8, 17 pp. [Available online at www.erh.noaa.gov/ssd/erps/ta/ta98-8.pdf.]

Blakeslee, R. J., and Coauthors, 2014: Lightning Imaging Sensor (LIS) for the International Space Station (ISS): Mission description and science goals. Extended Abstract, *15th Int. Conf. on Atmospheric Electricity*, Norman, OK, Earth Networks/Vaisala/Campbell Scientific, 0140011702. [Available online at http://ntrs.nasa.gov/archive/nasa/casi.ntrs.nasa.gov/20140011702.pdf.]

Boccippio, D. J., W. J. Koshak, and R. J. Blakeslee, 2002: Performance assessment of the optical transient detector and lightning imaging sensor. Part I: Predicted diurnal variability. *J. Atmos. Oceanic Technol.*, **19**, 1318–1332, doi:10.1175/1520-0426(2002)019<1318:PAOTOT>2.0.CO;2.

Briggs, M. S., and Coauthors, 2010: First results on terrestrial gamma-ray flashes from the Fermi gamma-ray burst monitor. *J. Geophys. Res.*, **115**, A07323, doi:10.1029/2009JA015242.

——, and Coauthors, 2013: Terrestrial gamma-ray flashes in the Fermi era: Improved observations and analysis methods. *J. Geophys. Res. Space Phys.*, **118**, 3805–3830, doi:10.1002/jgra.50205.

Carey, L. D., and S. A. Rutledge, 2000: On the relationship between precipitation and lightning in tropical island convection: A C-band polarimetric radar study. *Mon. Wea. Rev.*, **128**, 2687–2710, doi:10.1175/1520-0493(2000)128<2687:TRBPAL>2.0.CO;2.

Carlson, B. E., N. G. Lehtinen, and U. S. Inan, 2010: Terrestrial gamma ray flash production by active lightning leader channels. *J. Geophys. Res.*, **115**, A10324, doi:10.1029/2010JA015647.

Celestin, S., and V. P. Pasko, 2011: Energy and fluxes of thermal runaway electrons produced by exponential growth of streamers during the stepping of lightning leaders and in transient luminous events. *J. Geophys. Res.*, **116**, A03315, doi:10.1029/2010JA016260.

Cerniglia, C. S., and W. R. Snyder, 2002: Development of warning criteria for severe pulse thunderstorms in the northeastern United States using the WSR-88D. NOAA/National Weather Service Forecast Office Eastern Region Tech. Attachment 2002-03, 14 pp. [Available online at www.erh.noaa.gov/er/hq/ssd/erps/ta/ta2002-03.pdf.]

Christian, H. J., and Coauthors, 2003: Global frequency and distribution of lightning as observed from space by the optical transient detector. *J. Geophys. Res.*, **108**, 4005, doi:10.1029/2002JD002347.

Cohen, M. B., U. S. Inan, and G. Fishman, 2006: Terrestrial gamma ray flashes observed aboard the Compton Gamma Ray Observatory/Burst and Transient Source Experiment and ELV/VLF radio atmospherics. *J. Geophys. Res.*, **111**, D24109, doi:10.1029/2005JD006987.

——, ——, R. K. Said, and T. Gjestland, 2010: Geolocation of terrestrial gamma-ray flash source lightning. *Geophys. Res. Lett.*, **37**, L02801, doi:10.1029/2009GL041753.

Collier, A. B., T. Gjesteland, and N. Østgaard, 2011: Assessing the power law distribution of TGFs. *J. Geophys. Res.*, **116**, A10320, doi:10.1029/2011JA016612.

Connaughton, V., and Coauthors, 2010: Associations between Fermi Gamma-Ray Burst Monitor terrestrial gamma ray flashes and sferics from the World Wide Lightning Location Network. *J. Geophys. Res.*, **115**, A12307, doi:10.1029/2010JA015681.

——, and Coauthors, 2013: Radio signals from electron beams in terrestrial gamma-ray flashes. *J. Geophys. Res. Space Phys.*, **118**, 2313–2320, doi:10.1029/2012JA018288.

Cummer, S. A., Y. Zhai, W. Hu, D. M. Smith, L. I. Lopez, and M. A. Stanley, 2005: Measurements and implications of the relationship between lightning and terrestrial gamma ray flashes. *Geophys. Res. Lett.*, **32**, L08811, doi:10.1029/2005GL022778.

——, G. Lu, M. S. Briggs, V. Connaughton, S. Xiong, G. J. Fishman, and J. R. Dwyer, 2011: The lightning-TGF relationship on microsecond timescales. *Geophys. Res. Lett.*, **38**, L14810, doi:10.1029/2011GL048099.

——, and Coauthors, 2014: The source altitude, electric current, and intrinsic brightness of terrestrial gamma ray flashes. *Geophys. Res. Lett.*, **41**, 8586–8593, doi:10.1002/2014GL062196.

DeLobbe, L., and I. Holleman, 2006: Uncertainties in radar echo top heights used for hail detection. *Meteor. Appl.*, **13**, 361–374, doi:10.1017/S1350482706002374.

Dwyer, J. R., 2003: A fundamental limit on electric fields in air. *Geophys. Res. Lett.*, **30**, 2055, doi:10.1029/2003GL017781.

——, 2007: Relativistic breakdown in planetary atmospheres. *Phys. Plasmas*, **14**, 042901, doi:10.1063/1.2709652.

——, 2008: Source mechanisms of terrestrial gamma-ray flashes. *J. Geophys. Res.*, **113**, D10103, doi:10.1029/2007JD009248.

——, and D. M. Smith, 2005: A comparison between Monte Carlo simulations of runaway breakdown and terrestrial gamma-ray flash observations. *Geophys. Res. Lett.*, **32**, L22804, doi:10.1029/2005GL023848.

——, and S. A. Cummer, 2013: Radio emissions from terrestrial gamma-ray flashes. *J. Geophys. Res. Space Phys.*, **118**, 3769–3790, doi:10.1002/jgra.50188.

——, and M. A. Uman, 2014: The physics of lightning. *Phys. Rep.*, **534**, 147–241, doi:10.1016/j.physrep.2013.09.004.

——, and Coauthors, 2004: A ground level gamma-ray burst observed in association with rocket-triggered lightning. *Geophys. Res. Lett.*, **31**, L05119, doi:10.1029/2003GL018771.

——, D. M. Smith, and S. A. Cummer, 2012: High-energy atmospheric physics: Terrestrial gamma-ray flashes and related phenomena. *Space Sci. Rev.*, **173**, 133–196, doi:10.1007/s11214-012-9894-0.

Edwards, R., and R. L. Thompson, 1998: Nationwide comparisons of hail size with WSR-88D vertically integrated liquid water and derived thermodynamic sounding data. *Wea. Forecasting*, **13**, 277–285, doi:10.1175/1520-0434(1998)013<0277:NCOHSW>2.0.CO;2.

Fishman, G. J., and Coauthors, 1994: Discovery of intense gamma-ray flashes of atmospheric origin. *Science*, **264**, 1313–1316, doi:10.1126/science.264.5163.1313.

Gensini, V. A., and W. S. Ashley, 2011: Climatology of potentially severe convective environments from the North American Regional Reanalysis. *Electron. J. Severe Storms Meteor.*, **6** (8). [Available online at www.ejssm.org/ojs/index.php/ejssm/article/viewArticle/85.]

Gjesteland, T., N. Østgaard, A. B. Collier, B. E. Carlson, C. Eyles, and D. M. Smith, 2012: A new method reveals more TGFs in the RHESSI data. *Geophys. Res. Lett.*, **39**, L05102, doi:10.1029/2012GL050899.

——, ——, H. Christian, and A. Collier, 2015: Observation of a TGF from the convective core of a thundercloud. *Geophysical Research Abstracts*, Vol. 17, Abstract EGU2015-8750. [Available online at http://meetingorganizer.copernicus.org/EGU2015/EGU2015-8750.pdf.]

Goodman, S., and Coauthors, 2005: The North Alabama Lightning Mapping Array: Recent severe storm observations and future prospects. *Atmos. Res.*, **76**, 423–437, doi:10.1016/j.atmosres.2004.11.035.

——, and Coauthors, 2013: The GOES-R Geostationary Lightning Mapper (GLM). *Atmos. Res.*, **125–126**, 34–49, doi:10.1016/j.atmosres.2013.01.006.

Grefenstette, B. W., D. M. Smith, J. R. Dwyer, and G. J. Fishman, 2008: Time evolution of terrestrial gamma ray flashes. *Geophys. Res. Lett.*, **35**, L06802, doi:10.1029/2007GL032922.

——, ——, B. J. Hazelton, and L. I. Lopez, 2009: First RHESSI terrestrial gamma ray flash catalog. *J. Geophys. Res.*, **114**, A02314, doi:10.1029/2008JA013721.

Gurevich, A. V., G. M. Milikh, and R. Roussel-Dupre, 1992: Runaway electron mechanism of air breakdown and preconditioning during a thunderstorm. *Phys. Lett.*, **165A**, 463–468, doi:10.1016/0375-9601(92)90348-P.

Howard, K. W., J. J. Gourley, and R. A. Maddox, 1997: Uncertainties in WSR-88D measurements and their impacts on monitoring life cycles. *Wea. Forecasting*, **12**, 166–174, doi:10.1175/1520-0434(1997)012<0166:UIWMAT>2.0.CO;2.

Hutchins, M. L., R. H. Holzworth, J. B. Brundell, and C. J. Rodger, 2012: Relative detection efficiency of the World Wide Lightning Location Network. *Radio Sci.*, **47**, RS6005, doi:10.1029/2012RS005049.

Inan, U. S., S. C. Reising, G. J. Fishman, and J. M. Horack, 1996: On the association of terrestrial gamma-ray bursts with lightning and implications for sprites. *Geophys. Res. Lett.*, **23**, 1017–1020, doi:10.1029/96GL00746.

——, M. B. Cohen, R. K. Said, D. M. Smith, and L. I. Lopez, 2006: Terrestrial gamma ray flashes and lightning discharges. *Geophys. Res. Lett.*, **33**, L18802, doi:10.1029/2006GL027085.

King, M. D., S. Platnick, W. P. Menzel, S. A. Ackerman, and P. A. Hubanks, 2013: Spatial and temporal distribution of clouds observed by MODIS onboard the *Terra* and *Aqua* satellites. *IEEE Trans. Geosci. Remote Sens.*, **51**, 3826–3852, doi:10.1109/TGRS.2012.2227333.

Kitzmiller, D. H., W. E. McGovern, and R. F. Saffle, 1995: The WSR-88D severe weather potential algorithm. *Wea. Forecasting*, **10**, 141–159, doi:10.1175/1520-0434(1995)010<0141:TWSWPA>2.0.CO;2.

Klazura, G. E., and D. A. Imy, 1993: A description of the initial set of analysis products available from the NEXRAD WSR-88D system. *Bull. Amer. Meteor. Soc.*, **74**, 1293–1311, doi:10.1175/1520-0477(1993)074<1293:ADOTIS>2.0.CO;2.

Kokhanovsky, A., M. Vountas, and J. P. Burrows, 2011: Global distribution of cloud top height as retrieved from SCIAMACHY onboard ENVISAT spaceborne observations. *Remote Sens.*, **3**, 836–844, doi:10.3390/rs3050836.

Lay, E. H., 2008: Investigating lightning-to-ionosphere energy coupling based on VLF lightning propagation characterization. Ph.D. thesis, University of Washington, 126 pp.

Lenning, E., and H. E. Fuelberg, 1998: An evaluation of WSR-88D severe hail algorithms along the northeastern Gulf Coast. *Wea. Forecasting*, **13**, 1029–1045, doi:10.1175/1520-0434(1998)013<1029:AEOWSH>2.0.CO;2.

Liu, C., and S. Heckman, 2010: The application of total lightning detection and cell tracking for severe weather prediction. *TECO-2010 WMO Technical Conf. on Meteorological and Environmental Instruments and Methods of Observation*, Helsinki, Finland, WMO, P2(7).[Available online at www.wmo.int/pages/prog/www/IMOP/publications/IOM-104_TECO-2010/P2_7_Heckman_USA.pdf.]

——, E. J. Zipser, D. J. Cecil, S. W. Nesbitt, and S. Sherwood, 2008: A cloud and precipitation feature database from nine years of TRMM observations. *J. Appl. Meteor. Climatol.*, **47**, 2712–2728, doi:10.1175/2008JAMC1890.1.

Lu, G., and Coauthors, 2010: Lightning mapping observation of a terrestrial gamma-ray flash. *Geophys. Res. Lett.*, **37**, L11806, doi:10.1029/2010GL043494.

Marisaldi, M., and Coauthors, 2014: Properties of terrestrial gamma ray flashes detected by AGILE MCAL below 30 MeV. *J. Geophys. Res. Space Phys.*, **119**, 1337–1355, doi:10.1002/2013JA019301.

Meegan, C. A., and Coauthors, 2009: The Fermi Gamma-Ray Burst Monitor. *Astrophys. J.*, **702**, 791–804, doi:10.1088/0004-637X/702/1/791.

Mesinger, F., and Coauthors, 2006: North American Regional Reanalysis. *Bull. Amer. Meteor. Soc.*, **87**, 343–360, doi:10.1175/BAMS-87-3-343.

Neubert, T., 2009: ASIM—An instrument suite for the International Space Station. *AIP Conf. Proc.*, **1118**, 8, doi:10.1063/1.3137718.

Østgaard, N., T. Gjesteland, B. E. Carlson, A. B. Collier, S. A. Cummer, G. Lu, and H. J. Christian, 2013: Simultaneous observations of optical lightning and terrestrial gamma ray flash from space. *Geophys. Res. Lett.*, **40**, 2423–2426, doi:10.1002/grl.50466.

Price, C., 2008: Lightning sensors for observing, tracking and nowcasting severe weather. *Sensors*, **8**, 157–170, doi:10.3390/s8010157.

Rodger, C. J., J. B. Brundell, R. H. Holzworth, and E. H. Lay, 2009: Growing detection efficiency of the World Wide Lightning Location Network. AIP Conf. Proc., 1118, 15, doi:10.1063/1.3137706.

Saunders, C. P. R., 1993: A review of thunderstorm electrification processes. *J. Appl. Meteor.*, **32**, 642–655,

doi:10.1175/1520-0450(1993)032<0642:AROTEP>2.0.CO;2.

Setvák, M., and Coauthors, 2010: Satellite-observed cold-ring-shaped features atop deep convective clouds. *Atmos. Res.*, **97**, 80–96, doi:10.1016/j.atmosres.2010.03.009.

Shao, X.-M., T. Hamlin, and D. M. Smith, 2010: A closer examination of terrestrial gamma-ray flash-related lightning processes. *J. Geophys. Res.*, **115**, A00E30, doi:10.1029/2009JA014835.

Smith, D. M., L. I. Lopez, R. P. Lin, and C. P. Barrington-Leigh, 2005: Terrestrial gamma-ray flashes observed up to 20 MeV. *Science*, **307**, 1085–1088, doi:10.1126/science.1107466.

——, J. Hazelton, W. Grefenstette, J. R. Dwyer, R. H. Holzworth, and E. H. Lay, 2010: Terrestrial gamma ray flashes correlated to storm phase and tropopause height. *J. Geophys. Res.*, **115**, A00E49, doi:10.1029/2009JA014853.

Splitt, M. E., S. M. Lazarus, D. Barnes, J. R. Dwyer, H. K. Rassoul, D. M. Smith, B. Hazelton, and B. Grefenstette, 2010: Thunderstorm characteristics associated with RHESSI identified terrestrial gamma ray flashes. *J. Geophys. Res.*, **115**, A00E38, doi:10.1029/2009JA014622.

Stanley, M. A., X.-M. Shao, D. M. Smith, L. I. Lopez, M. B. Pongratz, J. D. Harlin, M. Stock, and A. Regan, 2006: A link between terrestrial gamma-ray flashes and intracloud lightning discharges. *Geophys. Res. Lett.*, **33**, L06803, doi:10.1029/2005GL025537.

Takahashi, T., 1973: Electrification of growing ice crystals. *J. Atmos. Sci.*, **30**, 1220–1224, doi:10.1175/1520-0469(1973)030<1220:EOGIC>2.0.CO;2.

Ushio, T., S. J. Heckman, D. J. Boccippio, H. J. Christian, and Z.-I. Kawasaki, 2001: A survey of thunderstorm flash rates compared to cloud top height using TRMM satellite data. *J. Geophys. Res.*, **106**, 24089–24095, doi:10.1029/2001JD900233.

Williams, E., V. Mushtak, D. Rosenfeld, S. Goodman, and D. Boccippio, 2005: Thermodynamic conditions favorable to superlative thunderstorm updraft, mixed phase microphysics and lightning flash rate. *Atmos. Res.*, **76**, 288–306, doi:10.1016/j.atmosres.2004.11.009.

——, and Coauthors, 2006: Lightning flashes conducive to the production and escape of gamma radiation to space. *J. Geophys. Res.*, **111**, D16209, doi:10.1029/2005JD006447.

Zipser, E. J., and K. R. Lutz, 1994: The vertical profile of radar reflectivity of convective cells: A strong indicator of storm intensity and lightning probability? *Mon. Wea. Rev.*, **122**, 1751–1759, doi:10.1175/1520-0493(1994)122<1751:TVPORR>2.0.CO;2.